Clothing Effect on Multilayered Skin Model Exposure From 20 GHz to 100 GHz

Kun Li, Kensuke Sasaki, Giulia Sacco, Maxim Zhadobov

Clothing Effect on Multilayered Skin Model Exposure From 20 GHz to 100 GHz

Kun Li, *Member, IEEE*, Kensuke Sasaki, *Member, IEEE*, Giulia Sacco, *Member, IEEE*, and Maxim Zhadobov, *Senior Member, IEEE*

***Abstract*—This study presents a statistical assessment of clothed human skin model exposure from 20 to 100 GHz. Dielectric property data for two typical textile materials, i.e., cotton and wool, were provided for the first time over the entire frequency range. A statistical analysis of the ratio of absorbed power density (APD) to skin temperature elevation was performed by Monte Carlo simulations using a multi-layer skin model with a textile layer. Three key parameters, namely the angle of incidence, cross-polarization power ratio (XPR), and air gap spacing between cloth and skin surface, were considered in the dosimetry analysis. The results show that at an incidence angle up to 60°, fluctuations of the ratio are observed by varying XPR from −50 to 50 dB. In the 20–100 GHz range, when the XPR is less than 0 dB, i.e., horizontally polarized wave is dominant, the impact on the ratio caused by either the incident angle or the air gap spacing is marginal. The deviation is increased when XPR exceeds 0 dB, i.e., vertically polarized wave is dominant, especially above 60 GHz at the incidence angles above 60°.**

***Index Terms*—APD, dielectric property, exposure assessment, millimeter waves, dosimetry, human skin, clothing effect, statistical analysis.**

I. Introduction

With the rapid development of the 5th/6th generation (5G/6G) wireless communication systems, millimeter-wave (mmWave) and terahertz (THz) frequencies are increasingly employed [1]. Wireless technologies and electronic/electrical devices operating at these frequencies, such as mobile phones, laptops, and wearable devices, should comply with electromagnetic fields (EMFs) exposure limits [2], [3]. In 2020 and 2019, the International Commission on Non-Ionizing Radiation Protection (ICNIRP) and the Institute of Electrical and Electronics Engineers (IEEE) International Commission on Electromagnetic Safety (ICES) (IEEE Standard C95.1) published the updated exposure limits [4], [5]. From 6 to 300 GHz, the revised guidelines/standard recommend the absorbed power density (APD) or epithelial power density, respectively, as a new metric for the basic restriction (BR) or dosimetric reference limit (DRL), which is derived from the threshold of adverse health effects related to superficial heating caused by localized EMF exposure.

Recent dosimetric studies on the APD at mmWaves primarily aimed at clarifying three aspects: 1) impact of beam steering upcoming for 5G/6G mobile systems; 2) appropriate APD averaging schemes or methods that enables high correlation with skin temperature elevation for distinct human body models; 3) clothing effects caused by textile materials that modify the electromagnetic power deposition in skin and resultant heating.

The angle-of-incidence dependence of the power transmission coefficient, APD, and skin temperature elevation induced by plane-wave exposure and practical radiation sources (e.g., phased array antennas) was extensively studied [6], [7], [8], [9], [10], [11]. Diao et al. clarified the effect of the incidence angle on the spatial-average power densities and resultant temperature elevation using both computational and thermographic measurement approaches [12], [13]. It was found that the normal incidence is the worst-case for surface temperature rise when bare skin is directly illuminated as it corresponds to the maximum APD for a given incident power density (IPD). Several groups computed APD and resultant temperature rise above 6 GHz using various skin models, exposure conditions and numerical methods [14], [15], [16], [17], [18], [19], [20], [21]. These computational results indicate that an APD ranging from 34–60 W/m^2 is required to elevate the temperature of bare skin by 1 °C.

On the other hand, the impact of clothing on skin exposure to mmWaves has garnered significant attention. At mmWaves, for the clothes that cover the human body, the dielectric properties of the fabric and an air gap spacing impact the electromagnetic power deposition [22], [23], [24], [25]. This may affect APD and resultant temperature elevation in the human skin. Sacco et al. studied APD and temperature rise at 26 and 60 GHz, considering the impact of a textile layer in contact or proximity of the human body [24], [25]. It is known that a textile material may perform as an impedance transformer, where an air gap between the cloth and skin modifies the electromagnetic power deposition and results in a temperature rise variation up to 20.9% compared to the bare skin at 60 GHz. However, the clothing effects on broadband mmWave skin exposure were not elucidated due to the lack of broadband complex permittivity data of textiles. Harmer et al. presented the complex permittivity of textiles and leather

Manuscript received 12 April 2023; revised 14 July 2023 and 14 August 2023; accepted 24 August 2023. *(Corresponding author: Kun Li.)*

Kun Li is with the Advanced Wireless and Communication Research Center (AWCC), The University of Electro-Communications, Tokyo 182-8585, Japan (e-mail: li.kun@awcc.uec.ac.jp).

Kensuke Sasaki is with the National Institute of Information and Communications Technology, Tokyo 184-8795, Japan (e-mail: k_sasaki@nict.go.jp).

Giulia Sacco and Maxim Zhadobov are with the Univ Rennes, CNRS, IETR (Institut d'Electronique et des Technologies du numeRique), UMR 6164, 35000 Rennes, France (e-mail: giulia.sacco@univ-rennes.fr; maxim.zhadobov@univ-rennes.fr).

Digital Object Identifier 10.1109/JERM.2023.3309935

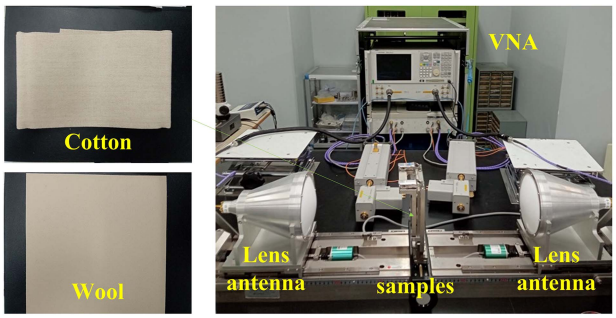

Fig. 1. Measurement setup for textile samples under test.

in 14–40 GHz using a free-wave transmittance-based method [26]. Luo et al. estimated the complex permittivities of four cloth materials (linen, leatherette, polyester fiber, and latex mattress) at 40–50 GHz based on quantum-behaved particle swarm optimization algorithm and free-space measurement [27]. At higher frequencies, since the air gap spacing is comparable with the wavelength, e.g., 3 mm at 100 GHz, it is indispensable to employ the broadband dielectric properties of cloths for accurate dosimetry analysis.

Another point worth discussing is what type of computational method is to be employed for dosimetric analysis of human body models covered with clothing. Numerical methods such as FDTD (finite-difference time-domain method) using whole-body voxel models are widely employed, but it is challenging to create a clothing model based on the existing body models, particularly at mmWaves. For localized exposure analysis using simplified models, the impact of textile material, configuration, thickness, and coverage method on the simulation accuracy is difficult to determine. Given the computational scale for mmWave bands, solving the one-dimensional multi-layer model using the Pennes bio-heat transfer equation is a practical and effective solution [22]. As a 1-D model, it may not realistically represent the three-dimensional thermal diffusion that occurs in the heterogeneous human body. However, since it is a rigorous solution obtained by solving the boundary conditions for both the electromagnetic field and heat conduction, the resulting skin temperature elevations up to steady-state may have more conservative values compared to numerical simulation results.

In this study, an equivalent dielectric property data for the samples of cotton and wool were measured for the first time. On the basis of measured dielectric constants, a statistical assessment of clothed human skin exposure at 20–100 GHz was performed by Monte Carlo simulation. The ratio between the APD and temperature elevation at the skin surface was analyzed using a multi-layer skin model with a textile layer.

II. Dielectric Property Measurement of Textile Samples

Fig. 1 shows the setup for measurement of dielectric properties of textile materials. The free-space method with spot-focus-type lens antennas was employed for measurements in the 18–110 GHz range [28]. Two lens antennas were connected to a vector network analyzer (E8361 A, Agilent Technologies) via a

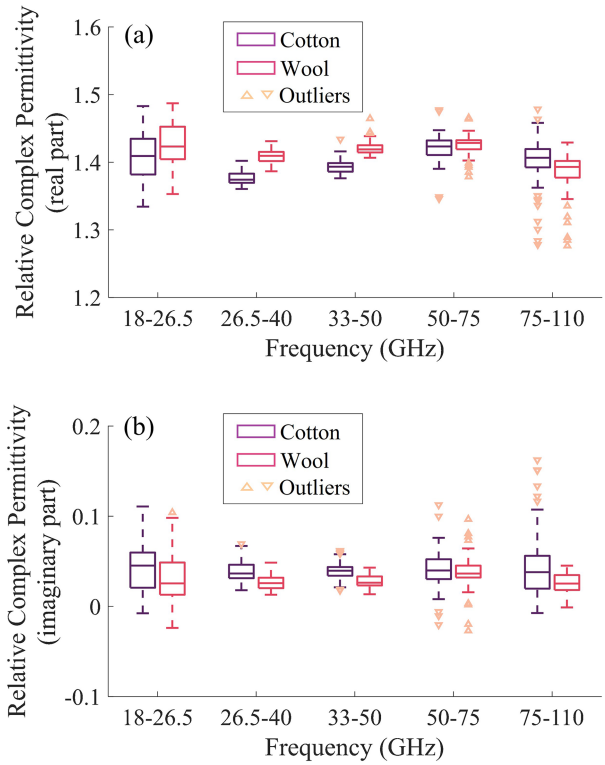

Fig. 2. Measured relative complex permittivity: (a) real part, (b) imaginary part.

mmWave frequency extender (N5260 A, Agilent Technologies). Measurements were conducted in K-, Ka-, Q-, V-, and W-bands, covering the frequency range of 18 to 110 GHz. During the experiment, a conical-rectangular waveguide adapter was utilized to facilitate the transition for each IEEE frequency band. TRL (Thru-Reflection-Line) calibration was applied before the start of each frequency band measurement. The reproducibility of our measurement system was checked using a reference sample, i.e., glass [28], before starting the measurement of clothing samples. Further details of the measurement procedure can be found in [28].

The box plots of measurement results for the samples of cotton and wool are shown in Fig. 2. Fig. 2(a) and (b) denote the real and imaginal part of relative complex permittivity, respectively, as a function of frequency. In Fig. 2(a) and (b), the height of the box indicates the interquartile range (IQR) from the 75th and 25th percentiles of entire data. The horizontal line in the middle of the box indicates the statistical median values of relative complex permittivities in each frequency range (K – W bands). The range between the lower and upper whiskers of the error bars represents the variability of the measured data within a range corresponding to 1.5 times IQR. The triangle signs indicate the outliers. The sampling intervals for the K-, Ka-, Q-bands were set at 250 MHz, while those for the V- and W-bands were set at 500 MHz. These intervals were primarily determined based on experience with dielectric permittivity measurements and the sweeping specifications of the test equipment. Therefore, for each box with error bars, the number of measurment points are 35, 55, 69, 51, 71 in each frequency band. It is observed that both

TABLE I
MEASURED COMPLEX PERMITTIVITY

cloth material	Re(ϵ_r*) mean ± std	Im(ϵ_r*) mean ± std
cotton	1.4 ± 0.03	0.03 ± 0.02
Ref. [24]	2	0.04
wool	1.42 ± 0.02	0.04 ± 0.02
Ref. [24]	1.22	0.036

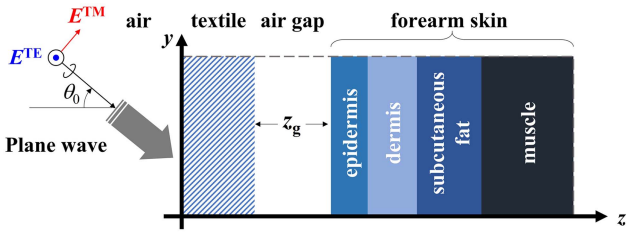

Fig. 3. Multilayer model used for statistical dosimetry analysis comprised of a cloth material, air gap layer, epidermis, dermis, fat, and muscle.

cotton and wool materials are almost non dispersive. Although outliers increase at higher frequencies, the statistical median value for both real and imaginary parts of complex permittivities are stable. This is mainly attributed to a negligibly small water concentration in the textile.

The statistical results of measured complex permittivities are summarized in Table I. Given the constant profiles of statistical median values for complex permittivities, as shown in Fig. 2, we use the average value of the data measured across the entire considered frequency band. The dielectric constant of textiles extracted in this study agrees well with those in [24]. Therefore, in this study, the mean value of permittivity of textile samples under test was employed to represent the equivalent dielectric constant for dosimetric analysis at 20–100 GHz. The simulation model and method are introduced hereafter.

III. ANALYTICAL MODEL AND METHOD

Fig. 3 shows a two-dimensional multilayer model representing human skin layers of the forearm covered by cloths. The model is composed of a textile material layer, an air gap, and a conventional four-layer skin model including epidermis, dermis, subcutaneous fat, and muscle layers [22]. The width of the air gap is z_g. A plane wave is used as excitation. The angle of incidence at the air/model interface is denoted as θ_0. Here, two polarization components are considered (TE and TM), whose electric field vectors are perpendicular and parallel to the incident plane, respectively. Thus, the cross-polarization power ratio of the incident wave, i.e., XPR, can be simplified as the power ratio of TE to TM waves in this 2-D model as follows.

$$XPR = \left(\frac{E^{\mathrm{TE}}}{E^{\mathrm{TM}}}\right)^2 \quad (1)$$

As mentioned in [22], this consideration is different from the empirical way of expressing XPR in multipath propagation environment of mobile communication systems. For dosimetric analysis, it is simplified by treating the multipath radio wave components as one illumination source before entering the human body. Therefore, the plane wave incidence does not take into account the phase difference between the orthogonally polarized components.

TABLE II
THERMAL PARAMETERS

layers	κ_i (W/(m°C))	ρ_i (kg/m^3)	A_i (W/m^3)	B_i (W/(m^3°C))
cotton	0.071	500	0	0
wool	0.054	500	0	0
air gap	0.027	1.13	0	0
epidermis	0.42	1109	1620	0
dermis	0.42	1109	1620	9100
subcutaneous fat	0.25	911	300	1700
muscle	0.50	1090	480	2700

The steady-state temperature elevation due to electromagnetic wave absorption considering the effects of cloths and air gap layers is calculated by solving Pennes's bioheat transfer equation [22], [29], [30], [31], [32],

$$\kappa_i \frac{d^2}{dz^2} T_i(z) + \sigma_i \frac{|E_i(z)|^2}{2} + A_i - B_i\left[T_i(z) - T_b\right] = 0, \quad (2)$$

where T_i and T_b are the temperatures of the each layer of skin models and blood (°C), respectively. κ_i is the thermal conductivity [W/(m ° C)]. A_i and B_i denote the basal metabolism per unit volume (W/m ^{3}) and a term associated with blood flow [W/(m^3° C)], respectively. σ_i denotes the equivalent conductivity (S/m) taking into account the dielectric loss. $E_i(z)$ is the peak amplitude of the electric field (V/m) inside the cloth materials, air gap spacing, and skin tissues.

The boundary conditions for thermal analysis of a clothed human skin model with and without an air gap space are described in detail in [22] ((3)–(14)). Note that the term associated with the electromagnetic power absorption $S_i(z)$ was derived considering the power allocation in the polarization components of incident waves,

$$S_i(z) = \frac{XPR}{1+XPR} S_{i,\mathrm{TE}}(z) + \frac{1}{1+XPR} S_{i,\mathrm{TM}}(z), \quad (3)$$

where the derivation of the formulae for the terms of $S_{i,\mathrm{TE}}(z)$ and $S_{i,\mathrm{TM}}(z)$ taking θ_0 and XPR into account is detailed (see Appendix in [22]). For consistency with previous studies [9], [22], [29], the dielectric properties of skin layers reported in [33], [34] were employed. The heat transfer coefficient for the air to skin boundary was set to 10 W/(m^2°C). The body core temperature at the deeper boundary of the muscle layer was set to 37 °C, and the air temperature was 20 °C. Table II summarizes the parameters used in the thermal analysis, inspired from the data reported in [24], [29]. IPD was set to 10 W/m^2.

Using the parameters and analytical formulae mentioned above, the variations of APD and temperature elevation at the clothed skin surface was evaluated by a Monte Carlo simulation. The Monte Carlo simulation was conducted by varying the thickness of each layer using normally distributed random numbers generated by Matlab R2019b [9]. The mean values and standard deviations of the thickness of cotton and wool materials were measured as 0.065 ± 0.015 mm and 1.24 ± 0.01 mm, respectively. The statistical data of the skin layer thicknesses in

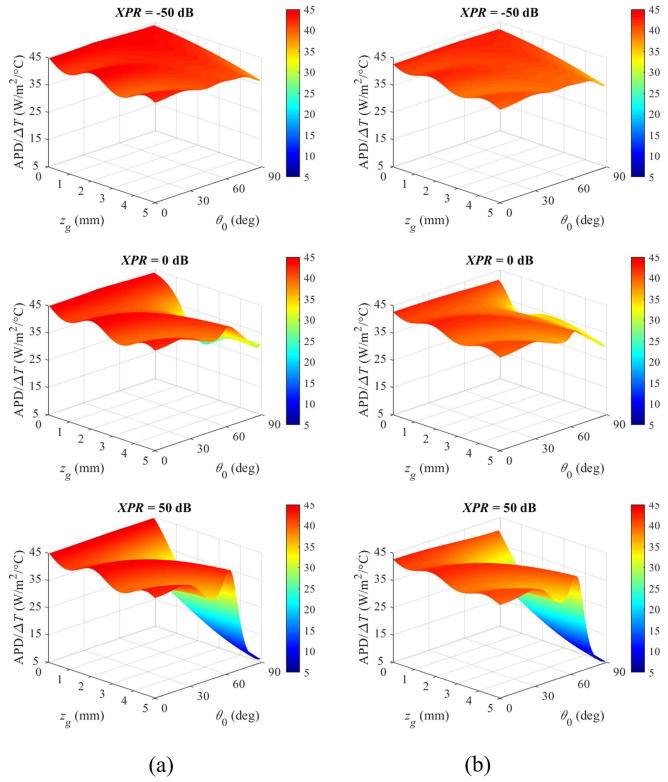

Fig. 4. Ratio of APD to ΔT at skin surface as functions of incidence angle (θ_0) and air gap spacing (z_g) at 60 GHz for selected values of XPR for (a) cotton and (b) wool.

previous study was employed (see Table II in [29]). The number of iterations was set to 10^4 for each oblique incidence angle, XPR, and air gap spacing.

IV. Results

A. Effects of XPR

Fig. 4 shows the mean ratio of the APD to the steady-state surface temperature elevation (ΔT) at 60 GHz as functions of θ_0 and z_g. The XPR at -50 dB, 0 dB, and 50 dB were shown, which denotes three representative scenarios: TM wave dominant; equal polarization power allocation; and TE wave dominant, respectively.

For both cotton (Fig. 4(a)) and wool (Fig. 4(b)) materials, all the results show a significant decrease at higher incidence angles and large air gap spacing, especially for cases of $XPR = 50$ dB. As θ_0 and z_g decrease to less than 60° or 3 mm, the ratio of the APD to ΔT remains at a relatively high level even with some fluctuations caused by the variations in incidence angle and air gap. When θ_0 is approaching 0°, i.e., normal incidence exposure, the increase in air gap spacing results in a periodic fluctuation. Moreover, it is observed that the fluctuation with the angle of incidence is relatively small in a radio-wave environment dominated by horizontally polarized incidence waves, i.e., $XPR = -50$ dB.

Fig. 5 illustrates the mean ratio of the APD to ΔT as a function of XPR when the angle of incidence θ_0 and air gap spacing z_g are under selected ranges at 20, 60, and 100 GHz. Fig. 5(a) and (b) show the results using cotton and wool materials, respectively. In Fig. 5(a), it is shown that the dependence on the XPR is not obvious at frequency of 20 GHz when θ_0 and z_g is less than 60° or 3 mm, respectively. When the frequency is increased to 60 GHz, a deviation can be observed when $XPR \geq 10$ dB. In particular, for cases of higher incidence angles, i.e., $\theta_0 = 60°$, a significant variation of the curves in the range of $XPR \geq 10$ dB is shown. Furthermore, at 100 GHz, the curve shows an abrupt decrease for the case of $\theta_0 = 60°$ at $z_g = 1$ mm in comparison with other cases.

For wool material, as shown in Fig. 5(b), almost similar profiles as those of cotton can be seen. At 60 GHz, a slight change occurs in some cases of $XPR > 0$ dB. However, most trends of curves indicate that when $XPR < 0$ dB, there is no obvious difference among all the results even considering the changes of θ_0 and z_g. When $XPR > 0$ dB, higher oblique incidence angle may result in a significant decrease of the ratio of the APD to ΔT. At lower frequency bands with lower angles of incidence, the ratio of the APD to ΔT is almost independent on the XPR.

B. Frequency Dependence

Fig. 6 shows the the mean ratio of the APD to ΔT as a function of frequency from 20 to 100 GHz under selected range of oblique incidence angle, i.e., $\theta_0 \leq 30°$ or $\theta_0 \leq 60°$. Fig. 6(a) and (b) indicate the results of cotton and wool materials, respectively, when $XPR \leq 0$ dB, i.e., $XPR = -50$, -20, -10, and 0 dB. Fig. 6(c) and (d) indicate the those when $XPR \geq 0$ dB, i.e., $XPR = 0$, 10, 20, and 50 dB. The air gap spacing z_g at the range of 0 to 5 mm were included. The error bars denote the standard deviation of the ratio of the APD to ΔT due to individual differences in the textile layer and skin tissue thickness.

As shown in Fig. 6(a) and (b), when $XPR \leq 0$ dB, the cases of $\theta_0 \leq 30°$ and $\theta_0 \leq 60°$ agree well with each other regardless of air gap spacing and textile materials. When $XPR \geq 0$ dB, as shown in Fig. 6(c) and (d), slight difference between the curves of $\theta_0 \leq 30°$ and $\theta_0 \leq 60°$ is observed. The statistical mean value indicates that the higher incidence angle up to 60° will result in a small decrease of the ratio of the APD to ΔT in a radio-wave environment dominated by vertically polarized incidence waves regardless of air gap spacing and cloth materials.

Fig. 7 shows the ratio of the APD to ΔT as a function of frequency from 20 to 100 GHz under selected range of air gap spacing, i.e., $z_g \leq 1$ mm or $z_g \leq 3$ mm. Fig. 7(a) and (b) indicate the results of cotton and wool materials, respectively, when $XPR \leq 0$ dB, whereas Fig. 7(c) and (d) indicate the those when $XPR \geq 0$ dB. The angle of incidence θ_0 ranging from 0 to 89° was considered. Similar to Fig. 6, the error bars denote the standard deviation due to individual differences in the textiles and skin tissue thickness.

When $XPR \leq 0$ dB, the curves of $z_g \leq 1$ mm and $z_g \leq 3$ mm show a small discrepancy with each other. This indicates that in a radio-wave environment dominated by horizontally polarized incidence waves, the difference of air gap spacing may have impact on the frequency dependence of ratio of the APD to ΔT at 20–100 GHz. On the other hand, when $XPR \geq 0$ dB, as shown in Fig. 7(c) and (d), a relatively large standard deviation occurs in the considered frequency range. With the increase of the air

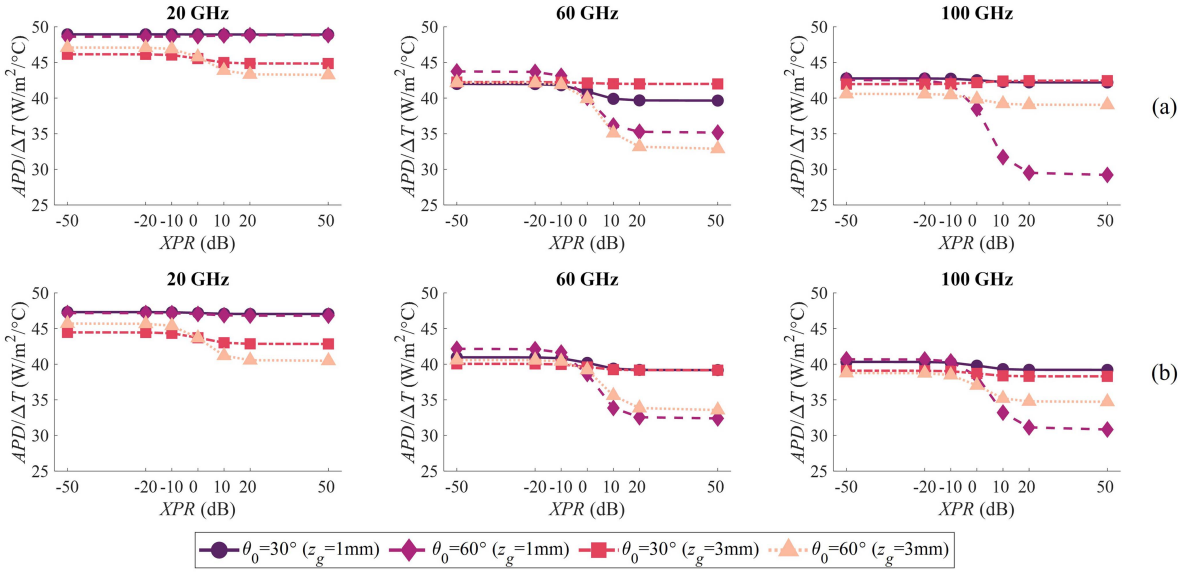

Fig. 5. Ratio of APD to ΔT at skin surface as a function of XPR under selected incidence angle (θ_0) and air gap spacing (z_g) at frequencies of 20, 60, and 100 GHz when using the textile materials of (a) cotton and (b) wool.

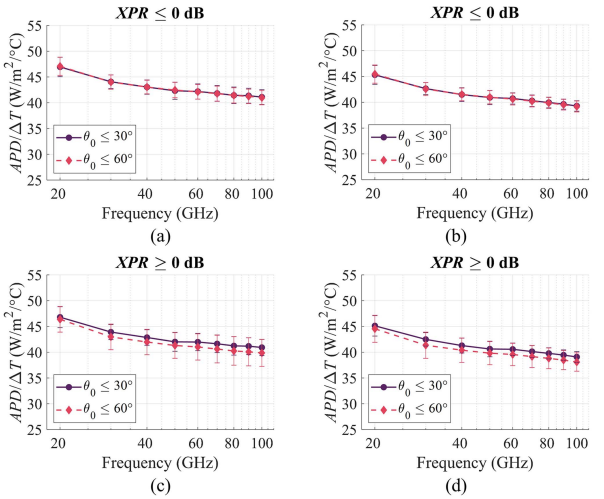

Fig. 6. Ratio of APD to ΔT at skin surface as a function of frequency under selected range of incidence angle (θ_0) at 20–100 GHz when (a) $XPR \leq 0$ dB (cotton), (b) $XPR \leq 0$ (wool), (c) $XPR \geq 0$ dB (cotton), and (d) $XPR \geq 0$ (wool).

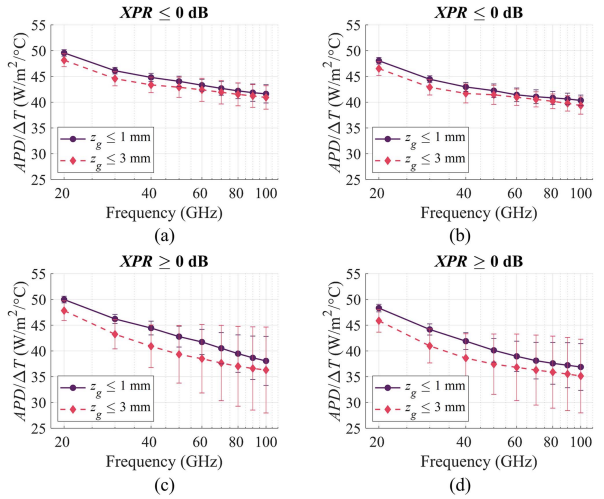

Fig. 7. Ratio of APD to ΔT at skin surface as a function of frequency selected range of air gap spacing (z_g) at 20–100 GHz when (a) $XPR \leq 0$ dB (cotton), (b) $XPR \leq 0$ (wool), (c) $XPR \geq 0$ dB (cotton), and (d) $XPR \geq 0$ (wool).

gap spacing range from $z_g \leq 1$ mm to $z_g \leq 3$ mm, the maximum relative standard deviation increases from 12.5% to 23%. This phenomenon may be attributed to the fact that many cases of extremely high incidence angles, i.e., over 60°, are included in the statistical outcomes. Comparing Figs. 6 and 7, it can be seen that the impacts on the ratio of the APD to ΔT caused by the air gap spacing may be higher than that by the oblique incidence angle when a relatively practical range of incidence angles is assumed, e.g., $\theta_0 \leq 60°$.

C. Statistical Analysis

Fig. 8 illustrates the probability density function (PDF) characteristics using the statistical mean values of the APD at frequencies from 20 to 100 GHz when the ΔT is assumed to be 0.5°. The histograms and fitted curves with Gaussian distribution are shown. Fig. 8(a) and (b) indicate the results of cotton and wool materials, respectively, when considering different selected range of incidence angles θ_0. Whereas Fig. 8(c) and (d) show those of considering the air gap spacing. The XPR was set from -50 to 50 dB.

In Fig. 8(a) and (b), it is observed that for each textiles, the histogram agrees approximately with the Gaussian distribution regardless of different ranges of incidence angles θ_0. However, in Fig. 8(c) and (d), small deviations from Gaussian distribution are shown when considering the selected range of the air gap spacing z_g.

The statistical results are summarized in Table III. For a selected range of angle of incidence or air gap spacing, all the other parameters such as XPR, frequency, and layer thickness

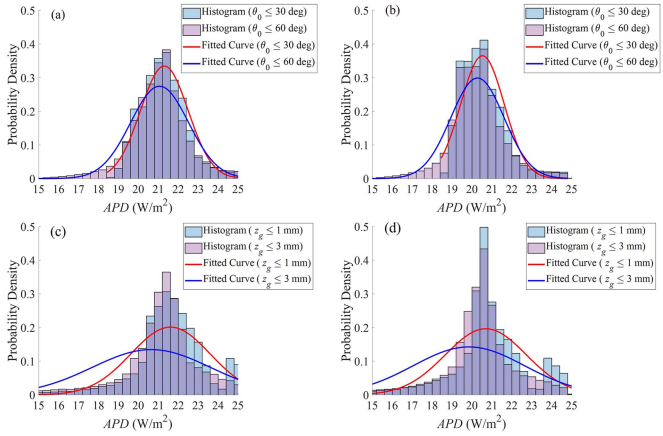

Fig. 8. PDF characteristics of APD when ΔT is 0.5° at 20–100 GHz with XPR from −50 to 50 dB for different textile materials under selected ranges of incidence angle and air gap spacing, (a) cotton ($\theta_0 \leq 30°$ and $\theta_0 \leq 60°$), (b) wool ($\theta_0 \leq 30°$ and $\theta_0 \leq 60°$), (c) cotton ($z_g \leq 1$ mm and $z_g \leq 3$ mm), and (d) wool ($z_g \leq 1$ mm and $z_g \leq 3$ mm).

TABLE III
STATISTICAL ANALYSIS

selected range	textile	mean ± std (W/m^2)	max MSE (W/m^2)	min MSE (W/m^2)	coeff.
$\theta \leq 30°$	cotton	21.30 ± 1.19	1.87	1.31	0.94
	wool	20.52 ± 1.09	1.90	1.31	0.90
$\theta \leq 60°$	cotton	21.06 ± 1.45	2.61	2.14	0.95
	wool	20.27 ± 1.33	2.59	2.09	0.94
$z_g \leq 1$mm	cotton	21.61 ± 1.98	2.82	2.46	0.89
	wool	20.69 ± 2.03	3.90	3.55	0.78
$z_g \leq 3$mm	cotton	20.65 ± 2.97	4.22	3.97	0.77
	wool	19.84 ± 2.80	4.91	4.65	0.75

variations were varied to derive the mean value and standard deviation of the APD that is required to elevate the 0.5 °C temperature elevation at skin surface. The mean square error (MSE) and correlation coefficient (coeff.) in comparison with Gaussian distribution are included. It can be seen that the mean values of the APD show a good agreement with the general public basic restriction of 20 W/m^2 for local exposure at 6–300 GHz in ICNIRP guideline [4]. In some cases, the required APD for the skin temperature elevation by 0.5 °C at high incident angles is smaller than the exposure limits in the ICNIRP guidelines, i.e., 20 W/m^2. This is actually because in order to obtain a large APD at high incident angles, an extremely higher level of IPD is required than at normal incidence. In other words, the APD will not exceed 20 W/m^2 when specifying the same IPD as in the Reference Levels in the ICNIRP guidelines. Moreover, the MSE range from 1.31–1.9 and 2.09–2.61, respectively, in the cases of $\theta_0 \leq 30°$ and $\theta_0 \leq 60°$. When the $z_g \leq 1$ mm and $z_g \leq 3$ mm is considered, the MSE increase to 2.46–3.9 and 3.97–4.91, respectively. The correlation coefficient also reduces from up to 0.95 to less than 0.75. The above-mentioned results imply that in the frequency range from 20 to 100 GHz, when the power allocation of polarization components were assumed for dosimetry analysis, to obtain an equivalent ΔT at the skin surface, the oblique incidence angle less than 60° do not significantly affect the statistical distribution of the APD even if the clothing effects were included. On the contrast, when the higher incidence angles were considered, the air gap spacing effects may result in a variation in the probability of the APD regardless of textile materials.

V. CONCLUSION

In this study, we investigated the statistical performance of clothed human-skin exposures to electromagnetic fields at 20–100 GHz. The equivalent dielectric constants for the textile materials of cotton and wool in the above frequency range was provided for the first time. Measurement results indicate that the frequency dependence of dielectric permittivities of the utilized cloth samples is relatively stable in the considered frequency range. Then, a statistical analysis of the ratio of the APD to skin surface temperature elevation using a multilayered skin model with textile and air gap layers was conducted by Monte Carlo simulation. The impacts of oblique incidence angles, XPR, and air gap spacing between textile layer and skin model were studied.

It is found that at a high incidence angle up to 60°, expectable fluctuations of the ratio of the APD to ΔT are observed when XPR range from −50 to 50 dB. At 20–100 GHz, when the XPR is less than 0 dB, i.e., horizontally polarized wave is dominant, the impact on the ratio of the APD to ΔT caused by either the incident angle or the air gap spacing is not significant. The deviation of the ratio of the APD to ΔT will be increased when XPR exceeds 0 dB, i.e., vertically polarized wave is dominant, especially at frequencies over 60 GHz when the incidence angle is higher than 60°. However, considering more realistic exposure conditions in general, such as incident angles less than 60° and air gaps less than 3 mm, it is observed that the impact on the APD to obtain an equivalent ΔT caused by the clothing effects in the above frequency range is marginal from statistics point of view.

REFERENCES

[1] M. Zhadobov, N. Chahat, R. Sauleau, C. L. Quement, and Y. L. Drean, "Millimeter-wave interactions with the human body: State of knowledge and recent advances," *Int. J. Microw. Wireless Technol.*, vol. 3, no. 2, pp. 237–247, Mar. 2011.

[2] A. Hirata et al., "Assessment of human exposure to electromagnetic fields: Review and future directions," *IEEE Trans. Electromagn. Compat.*, vol. 63, no. 5, pp. 1619–1630, Oct. 2021.

[3] T. Wu et al., "Editorial: Human exposure to new-emerging electric, magnetic and electromagnetic fields," *Front. Public Health - Radiat. Health*, vol. 10, Apr. 2022, Art. no. 894624.

[4] International Commission on Non-Ionizing Radiation Protection (ICNIRP), "Guidelines for limiting exposure to time-varying electric, magnetic and electromagnetic fields (100 kHz to 300 GHz)," *Health Phys.*, vol. 118, no. 5, pp. 483–524, May, 2020.

[5] *IEEE Standard for Safety Levels with Respect to Human Exposure to Radio Frequency Electromagnetic Fields, 0 Hz to 300 GHz*, Standard IEEE C95.1-2019, New York, NY, USA, 2019.

[6] M. Zhadobov, C. Leduc, A. Guraliuc, N. Chahat, and R. Sauleau, "Antenna/human body interactions in the 60 GHz band: State of knowledge and recent advances," *Adv. Body-Centric Wireless Commun.: Appl. State-of-The-Art, IET*, pp. 97–142, Jun. 2016.

[7] K. Li et al., "Intercomparison of calculated incident power density and temperature rise for exposure from different antennas at 10–90 GHz," *IEEE Access*, vol. 9, pp. 151654–151666, 2021.

[8] T. Wu, T. S. Rappaport, and C. M. Collins, "Safe for generations to come: Considerations of safety for millimeter waves in wireless communications," *IEEE Microw. Mag.*, vol. 16, no. 2, pp. 65–84, Mar. 2015.
[9] K. Li, K. Sasaki, S. Watanabe, and H. Shirai, "Relationship between power density and surface temperature elevation for human skin exposure to electromagnetic waves with oblique incidence angle from 6 GHz to 1 THz," *Phys. Med. Biol.*, vol. 64, no. 6, Mar. 2019, Art. no. 065016.
[10] W. He, B. Xu, M. Gustafsson, Z. Ying, and S. He, "RF compliance study of temperature elevation in human head model around 28 GHz for 5G user equipment application: Simulation analysis," *IEEE Access*, vol. 6, pp. 830–838, 2018.
[11] T. Nakae, D. Funahashi, J. Higashiyama, T. Onishi, and A. Hirata, "Skin temperature elevation for incident power densities from dipole arrays at 28 GHz," *IEEE Access*, vol. 8, pp. 26863–26871, 2020.
[12] Y. Diao et al., "Effect of incidence angle on the incident power density definition to correlate skin temperature rise for millimeter wave exposures," *IEEE Trans. Electromagn. Compat.*, vol. 63, no. 5, pp. 1709–1716, Oct. 2021.
[13] *IEEE Guide for the Definition of Incident Power Density to Correlate Surface Temperature Elevation*, IEEE Standard 2889, Dec. 2021.
[14] D. Funahashi, A. Hirata, S. Kodera, and K. R. Foster, "Area-averaged transmitted power density at skin surface as metric to estimate surface temperature elevation," *IEEE Access*, vol. 6, pp. 77665–77674, 2018.
[15] Y. Diao, E. A. Rashed, and A. Hirata, "Assessment of absorbed power density and temperature rise for nonplanar body model under electromagnetic exposure above 6 GHz," *Phys. Med. Biol.*, vol. 65, no. 22, Nov. 2020, Art. no. 224001.
[16] K. Li, K. Sasaki, K. Wake, T. Onishi, and S. Watanabe, "Quantitative comparison of power densities related to electromagnetic near-field exposures with safety guidelines from 6 to 100 GHz," *IEEE Access*, vol. 9, pp. 115801–115812, 2021.
[17] G. Sacco, Z. Haider, and M. Zhadobov, "Exposure levels induced in curved body parts at mmWaves," *IEEE J. Electromagnetics, RF Microw. Med. Biol.*, vol. 6, no. 3, pp. 413–419, Sep. 2022.
[18] K. Taguchi, S. Kodera, A. Hirata, and T. Kashiwa, "Computation of absorbed power densities in high-resolution head models by considering skin thickness in quasi-millimeter and millimeter wave bands," *IEEE J. Electromagnetics, RF Microw. Med. Biol.*, vol. 6, no. 4, pp. 516–523, Dec. 2022.
[19] S. Kodera et al., "Whole-body exposure system using horn antennas with dielectric lens at 28 GHz," *IEEE J. Electromagnetics, RF Microw. Med. Biol.*, vol. 7, no. 1, pp. 65–72, Mar. 2023.
[20] M. Yao, S. S. Zhekov, B. Xu, K. Li, and S. Zhang, "A study on exposure to electromagnetic fields from user equipment antennas above 100 GHz," *IEEE Trans. Electromagn. Compat.*, early access, Apr. 19, 2023, doi: 10.1109/TEMC.2023.3262322.
[21] K. Li et al., "Calculated epitherial/absorbed power density for exposure from antennas at 10–90 GHz: Intercomparison study using planar skin modela," *IEEE Access*, vol. 11, pp. 7420–7435, 2023.
[22] K. Li, "Multivariate regression analysis of skin temperature rises for millimeter-wave dosimetry," *IEEE Trans. Electromagn. Compat.*, vol. 64, no. 4, pp. 941–950, Aug. 2022.
[23] K. Li and K. Sasaki, "Monte Carlo simulation of clothed skin exposure to electromagnetic field with oblique incidence angles at 60 GHz," *Front. Public Health - Radiat. Health*, vol. 10, pp. 1–8, Feb. 2022.
[24] G. Sacco, S. Pisa, and M. Zhadobov, "Impact of textile on electromagnetic power and heating in near-surface tissues at 26 GHz and 60 GHz," *IEEE J. Electromagn., RF, Microw. Med. Biol.*, vol. 5, no. 3, pp. 262–268, Sep. 2021.
[25] G. Sacco, D. Nikolayev, R. Sauleau, and M. Zhadobov, "Antenna/human body coupling in 5 G millimeter-wave bands: Do age and clothing matter?," *IEEE J. Microw.*, vol. 1, no. 2, pp. 593–600, Apr. 2021.
[26] N. Rezgui, N. Bowring, Z. Luklinska, S. Harmer, and G. Ren, "Determination of the complex permittivity of textiles and leather in the 14–40 GHz millimetre-wave band using a free-wave transmittance only method," *Microw., Antennas Propag.*, vol. 2, no. 6, pp. 606–614, Sep. 2008.
[27] J. Luo, Y. Shao, X. Liao, J. Liu, and J. Zhang, "Complex permittivity estimation for cloths based on QPSO method over (40 to 50) GHz," *IEEE Trans Antennas Propag.*, vol. 69, no. 1, pp. 600–605, Jan. 2021.
[28] K. Sasaki, H. Segawa, M. Mizuno, K. Wake, S. Watanabe, and O. Hashimoto, "Development of the complex permittivity measurement system for high-loss biological samples using the free space method in quasi-millimeter and millimeter wave bands," *Phys. Med. Biol.*, vol. 58, no. 5, pp. 1625–1633, Feb. 2013.
[29] K. Sasaki, K. Wake, and S. Watanabe, "Monte carlo simulations of skin exposure to electromagnetic field from 10 GHz to 1 THz," *Phys. Med. Biol.*, vol. 62, no. 17, pp. 6993–7010, Aug. 2017.
[30] K. Sasaki, K. Li, and T. Nagaoka, "Human skin exposure to terahertz waves from 0.1 to 1 THz: Statistical assessments using multilayered planar models," in *Proc. IEEE Int. Microw. Biomed. Conf.*, Suzhou, China, 2022, pp. 25–27.
[31] A. Kanezaki, A. Hirata, S. Watanabe, and H. Shirai, "Parameter variation effects on temperature elevation in a steady-state, one-dimensional thermal model for millimeter wave exposure of one-and three-layer human tissue," *Phys. Med. Biol.*, vol. 55, no. 16, pp. 4647–4659, 2010.
[32] A. Hirata et al., "Human exposure to radiofrequency energy above 6 GHz: Review of computational dosimetry studies," *Phys. Med. Biol.*, vol. 66, no. 8, Apr. 2021, Art. no. 08TR01.
[33] K. Sasaki, K. Wake, and S. Watanabe, "Measurement of the dielectric properties of the epidermis and dermis at frequencies from 0.5 GHz to 110 GHz," *Phys. Med. Biol.*, vol. 59, no. 16, pp. 4739–4747, Aug. 2014.
[34] "NICT database of tissue dielectric properties for electromagnetic modeling of human body," Mar. 2023. [Online]. Available: https://www2.nict.go.jp/cgi-bin/202303080003/public_html/index.py

Kun Li (Member, IEEE) received the B.E. degree in communication engineering from the Nanjing University of Posts and Telecommunications, Nanjing, China, in 2011, and the M.E. and Ph.D. degrees in electrical engineering from the University of Toyama, Toyama, Japan, in 2014 and 2017, respectively. From 2017 to 2019, he was a Researcher with the Electromagnetic Compatibility Laboratory, National Institute of Information and Communications Technology, Tokyo, Japan. From 2020 to 2023, he was an Assistant Professor with the Faculty of Engineering and Design, Kagawa University, Takamatsu, Japan. He was a Visiting Researcher with the CNRS/IETR, University of Rennes 1, Rennes, France, from 2022 to 2023. In 2023, he joined the Advanced Wireless and Communication Research Center, The University of Electro-Communications, Tokyo, Japan, where he is currently working as an Associate Professor. His research interests include electromagnetic computation and measurement for radiation safety by human exposure to electromagnetic fields in radio frequencies, antenna design and measurement techniques for wireless body area network system. He was the recipient of the Young Scientist Award of the URSI, in 2020, the Risaburo Sato Award of EMC Sapporo & AMPEC, in 2019, the IEEE AP-S Japan Student Award in 2015, and the IEICE Best Letter Award in 2017. He is currently the Early Career Representative of URSI Commision K, and the Co-Chair of Working Group under Subcommittee 6, the IEEE International Committee on Electromagnetic Safety (ICES) TC-95 since 2022. He is a senior member of URSI and IEICE.

Kensuke Sasaki (Member, IEEE) received the B.E., M.E., and Ph.D. degrees in electrical and electronic engineering from Tokyo Metropolitan University, Tokyo, Japan, in 2006, 2008, and 2011, respectively. He is currently a Senior Researcher with the Electromagnetic Compatibility Laboratory, Electromagnetic Standards Research Center, Radio Research Institute, National Institute of Information and Communications Technology, Japan. He is also a Visiting Associate Professor with the Nagoya Institute of Technology, Nagoya, Japan, from 2022. His research interests include electromagnetic theory, bioelectromagnetics, and dielectric properties measurement. Dr. Sasaki was a member of Scientific Expert Group of International Commission on Non-Ionizing Radiation Protection (ICNIRP) from 2018 to 2020. He has been the Early Carrier Representative of Commission K, the International Scientific Radio Union (URSI) since 2017. He is the Co-Chair of Working Group six under Subcommittee six, the IEEE International Committee on Electromagnetic Safety (ICES) TC-95 since 2022. He was the recipient of the 2009 Young Scientist Award of the URSI, the 2012 Best Paper Award of the IEEJ, and the 2020 Achievement Award of the IEICE.

Giulia Sacco (Member, IEEE) received the M.S. degree (*summa cum laude*) in biomedical engineering and the Ph.D. degree (*cum laude* and with the Doctor Europaeus label) in information and communication technology from the Sapienza University of Rome, Rome, Italy, in 2017 and 2021, respectively. She was a Visiting Researcher with Stiching imec, Eindhoven, The Netherlands, from April 2019 to September 2019. She is currently a Researcher and a Marie Curie Fellow with the Institut d'Électronique et des Technologies du numérique/French National Center for Scientific Research (CNRS), Rennes, France. Her research interests include the field of innovative biomedical applications of electromagnetic fields and radars for vital signs monitoring. Dr. Sacco was the recipient of the Young Scientist Award at the XXXV General Assembly and Scientific Symposium (GASS) of the International Union of Radio Science (Union Radio Scientifique Internationale-URSI) 2023, 2022 Antennas and Propagation Society (AP-S) Fellowship, Bourse de Jeunes Chercheurs Grant at the XXXIV URSI GASS 2021, the Best Student Paper Award at the XXXIII URSI GASS 2020, and the Best Student Paper Award at the Photonics & Electromagnetics Research Symposium (PIERS) 2019.

Maxim Zhadobov (Senior Member, IEEE) received the Ph.D. and Habilitation á Diriger des Recherches degrees from the Institut d'Electronique et des Technologies du numerique (IETR), University of Rennes 1, Rennes, France, in 2006 and 2016, respectively. He was a Postdoctoral Researcher with the Center for Biomedical Physics, Temple University, Philadelphia, PA, USA, till 2008, and then joined the French National Center for Scientific Research (CNRS). He is currently a Senior Research Scientist with the IETR/CNRS in charge of the Electromagnetic Waves in Complex Media (eWAVES) Research Group. He has coauthored five book chapters, 85 research papers in peer-reviewed international journals, and more than 200 contributions to conferences and workshops. His research interests include innovative biomedical applications of electromagnetic fields and associated technologies. His review article in the *International Journal of Microwave and Wireless Technologies* has been the most cited paper since 2016. A paper published by his research group in 2019 is in journal Top 100 of Nature Scientific Reports. He has been involved in 26 research projects (14 as PI). Dr. Zhadobov was the TPC Co-Chair of BioEM 2021/2020. He was the TPC member and/or session organizer at international conferences, including AES 2023, EUMW2022, IEEE IMBioC 2022, AT-AP-RASC 2022, BioEM 2019, EuMW 2019, IEEE iWEM 2017, MobiHealth 2015–2017, BodyNets 2016, and IMWS-Bio 2014. He was an elected member of EBEA Council from 2017 to 2021. He is currently the president of URSI France Commission K and member of IEEE TC95.4. He is an Associate Editor for IEEE JOURNAL OF ELECTROMAGNETICS, RF AND MICROWAVES IN MEDICINE AND BIOLOGY and was the Guest Editor of several special issues, including Human Exposure in 5G and 6G Scenarios of Applied Sciences and Advanced Electromagnetic Biosensors for Medical, Environmental and Industrial Applications of Sensors. He was also on review boards of more than 15 international journals and conferences, and has been acting as an expert at research councils worldwide. He was the recipient of the Research & Innovation Award from BPGO in 2022, CNRS Medal in 2018, the EBEA Award for Excellence in Bioelectromagnetics in 2015, and Brittany's Young Scientist Award in 2010. Since 2010, the Ph.D. students worked and have been recipients of seven national scientific awards and six awards from the Bioelectromagnetics Society, URSI, IEEE Antennas and Propagation and IEEE Microwave Theory and Technology Societies.